FISEVIER

Contents lists available at ScienceDirect

# Nuclear Inst. and Methods in Physics Research, A

journal homepage: www.elsevier.com/locate/nima



# Parametrization of high light yield, energy resolution, and optical cross-talk in SiPM-based liquid argon detectors



A. Moharana a, C. Galbiati a,b, S. Horikawa a,c,\*, P. Kachru a, I. Kochanek d, K. Kondo c,d, A. Razeto d

- <sup>a</sup> Gran Sasso Science Institute, Viale Francesco Crispi, 7, L'Aquila, 67100, Italy
- <sup>b</sup> Physics department, Princeton University, Princeton, NJ, 08544, USA
- c Department of Industrial and Information Engineering and Economics, Università degli Studi dell'Aquila, L'Aquila, 67100, Italy
- d INFN Laboratori Nazionali del Gran Sasso, Assergi, L'Aquila, 67100, Italy

#### ARTICLE INFO

#### Keywords: Liquid argon detector Light yield SiPM Cross-talk

#### ABSTRACT

Liquefied noble gases are widely used as detector media in various physics experiments owing to their high scintillation efficiency and ease of scalability to large volumes. Now-a-days, these experiments are gradually shifting to SiPM-based readouts because of their high photon detection efficiency, superior resolution, and relative ease of use. However, SiPMs emit photons during the avalanche process, known as optical cross-talk, which can significantly affect the measured signal. In this work, we present two small single-phase liquid argon chambers equipped with SiPM arrays. They display high gross light yields up to 32 photo-electrons per keV, with ~12 attributed to primary photo-electrons generated by scintillation photons. We then present the full parametrization of the over-voltage dependence of the light yield, energy resolution, and optical cross-talk, based on dedicated measurements of optical cross-talk components and a simple analytical model.

### 1. Introduction

A Geiger discharge in a microcell of a SiPM emits isotropically a few tens of photons [1,2] that have enough energy to create an electronhole (e-h) pair in silicon. These photons can create a charge pair in, or close to the avalanche region of another microcell of the SiPM. Thereafter, one of the charge carriers from such an e-h pair may trigger a secondary avalanche, known as optical cross-talk (oCT). In nobleliquid detectors, scintillation photons generated following a particle interaction form the signal for the photo-sensors. However, the oCT in/between the SiPMs in the setup amplifies the original signal, affecting the energy or position reconstruction resolution [3,4]. Therefore, detailed characterization of the oCT components is of paramount importance for SiPM-based light readout system. In this paper we classify three types of oCT observed in a detector system with multiple readout channels, each comprising an array of SiPMs. If the photon remains confined in the Si bulk and produces an avalanche in a neighboring cell, it is called internal cross-talk (iCT). Alternatively, if the photon escapes from the Si bulk and produces an avalanche in another SiPM array, it is called external cross-talk (eCT). If the photon is reflected back and absorbed by the same SiPM array which emitted it, it is called feedback cross-talk (fCT). While the eCT and fCT probability largely depends on the detector optics, iCT is an intrinsic property of the SiPMs. In the following sections we present the parametrization of the over-voltage

(OV) dependence of the light yield, energy resolution, and optical crosstalk of two small liquid argon (LAr) detector prototypes equipped with SiPM arrays. Comprehensive discussions on the oCT analysis on the presented data set is reported also in Ref. [5].

#### 2. Experimental setup

# 2.1. Cryogenic setup and calibration sources

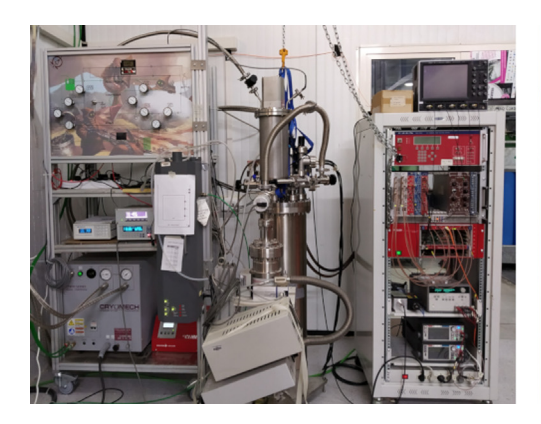
Fig. 1 (Left) shows the cryogenic setup [6] that was used for hosting the detectors under study. The detectors were installed inside a stainless steel vessel which was then filled with 4 L of LAr using a pulse-tube cryocooler. The system consists of a closed circulation loop of gaseous argon that is maintained at a volumetric flow of 6 SL/min, along with a SAES PS4-MT3 getter for continuous purification of the argon boil-off. Two radioactive sources were used for performing energy calibration measurements. Metastable <sup>83m</sup>Kr atoms were injected into the re-circulation loop, providing a calibration line at 41.5 keV. An <sup>241</sup>Am source, which emits 59.5 keV gamma-photons, was attached to the outer wall of the cryostat.

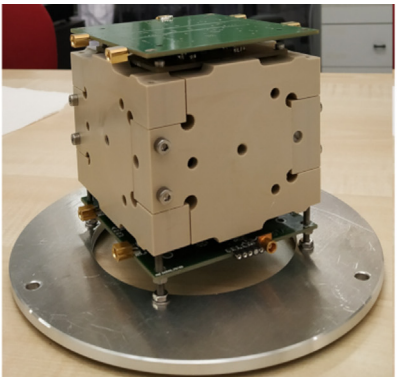
# 2.2. Cubic chamber

Fig. 1 (Center) shows the cubic chamber whose walls were machined from polyetheretherketone (PEEK). The inner surfaces of the

E-mail address: sosuke.horikawa@gssi.it (S. Horikawa).

Corresponding author.





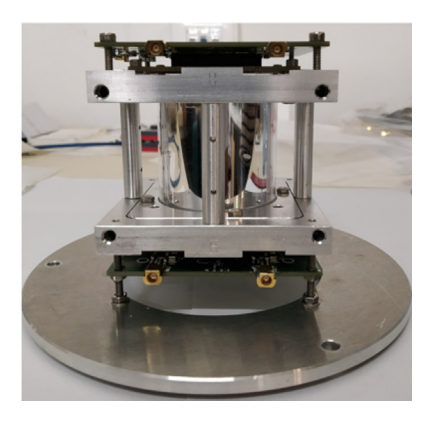


Fig. 1. (Left) Cryogenic setup; (Center) Cubic chamber with inner dimensions  $50 \times 50 \times 50 \times 8$  mm<sup>3</sup>; (Right) Cylindrical chamber with inner dimensions  $46 \times 50$  mm<sup>2</sup> ( $\phi \times h$ ).

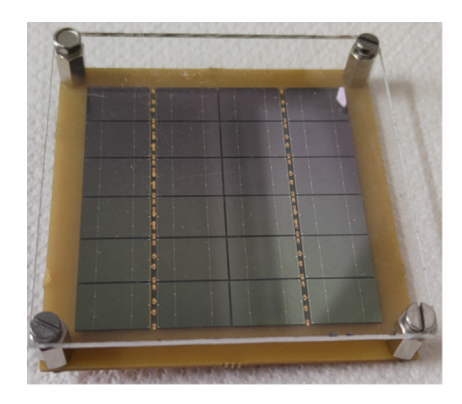




Fig. 2. (Left) SiPM Tile with dimensions  $5 \times 5 \text{ cm}^2$ ; (Right) Front-end electronics board with four readout channels.

side walls are lined with Vikuiti Enhanced Specular Reflector (ESR) foils from 3M, and the top and bottom faces have fused silica windows. The active argon volume has the dimensions  $50\times50\times50.8~\text{cm}^3$ . All internal surfaces are coated with tetraphenyl butadiene (TPB) for wavelength shifting of the Ar scintillation photons (128 nm) to visible range. The visible photons are then detected by two  $5\times5~\text{cm}^2$  SiPM arrays installed on top of the fused silica windows.

# 2.3. Cylindrical chamber

Fig. 1 (Right) shows the cylindrical chamber that is realized in 2-mm thick polymethyl methacrylate (PMMA), and internally lined with a TPB coated ESR foil. Two TPB-coated fused silica windows are installed on the top and bottom faces, along with the same SiPM arrays that were used in the cubic chamber. The inner volume dimensions measure  $46\times50~\text{mm}^2~(\phi\times\text{h}).$ 

# 3. Photo-detectors & readout

Fig. 2 (Left) shows a SiPM tile, which is an array of 24 SiPMs from the FBK NUV-HD-Cryo family. Fig. 2 (Right) shows a front-end electronics board (FEB), consisting of four cryo-grade low-noise transimpedance amplifiers (TIA), each amplifying the summed output from six SiPMs. The four TIA output channels are individually read out, however, all the analyses presented in this paper are performed on the sum of the four readout channels of each tile. A copy of the signals is sent to a set of NIM electronics to form the trigger logic, following which the data is acquired with a CAEN V1720 digitizer unit. For the SiPM gain calibration an optical fiber connected to a 405 nm laser system is inserted into the chambers. Data is then acquired in the OV range of (1.0–9.5) V.

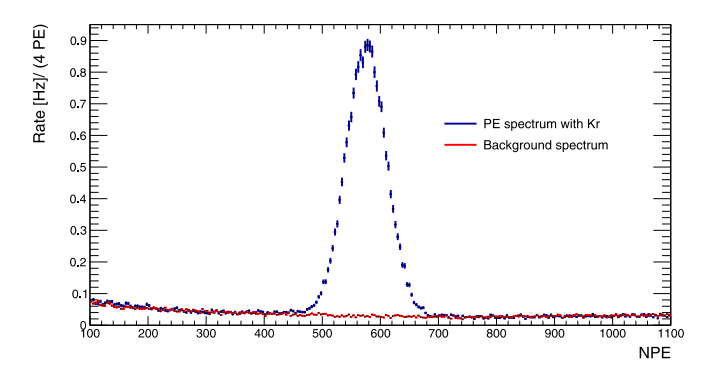
# 4. Data analysis

#### 4.1. Gross light yield and energy resolution

Fig. 3 (Left) shows the  $^{83\text{m}}$ Kr photo-electron spectrum and the background spectrum at 5.5 OV. A Gaussian model is fitted to the background subtracted spectra to extract the mean number of photo-electrons observed at a particular OV. The gross light yield (LY<sub>G</sub>) is calculated from the ratio of the detected photo-electrons and the energy deposited in the medium. Fig. 3 (Right) shows the LY<sub>G</sub> as a function of the applied OV for both chambers. The mean LY<sub>G</sub> increases from 5 pe/keV at 1.0 OV to 32 pe/keV at 9.5 OV, in both chambers. Additionally, similar values are obtained with  $^{83\text{m}}$ Kr and  $^{241}$ Am. Similarly, the gross energy resolution ( $\sigma_G$ ) is determined from the ratio of standard deviation and mean of the fitted Gaussian model. It is found to improve with increasing OV initially, however, it starts worsening again at higher OVs (see Fig. 5 right). This is a clear indication of the fact that the large increase in the LY<sub>G</sub> at higher OVs is because of significant contributions from oCT.

#### 4.2. Internal cross-talk

As iCT is an intrinsic property of the SiPMs, it was parametrized through a separate measurement in liquid nitrogen, with a single SiPM exposed to low-intensity laser pulses [5]. Reflections were suppressed using black tapes and hence the fCT contribution was negligible. The photo-electron distribution thus obtained can be assumed as a convolution of the probability density function of iCT (with the mean  $\mu_{\rm iCT}$ ) and the Poisson distribution (mean  $\epsilon$ ) of the detected laser photons. The observed mean value  $\langle n \rangle$  is then given as  $\langle n \rangle = \mu_{\rm iCT} \cdot \epsilon$ ; with  $\epsilon = -\ln(R_0)$ ,  $R_0$  being the relative population of the zero photo-electron peak. Assuming that the iCT generation is described by a geometric series [3] with the common ratio  $\lambda_{\rm iCT} \ll 1$ ,  $\mu_{\rm iCT} = 1/(1-\lambda_{\rm iCT})$ .



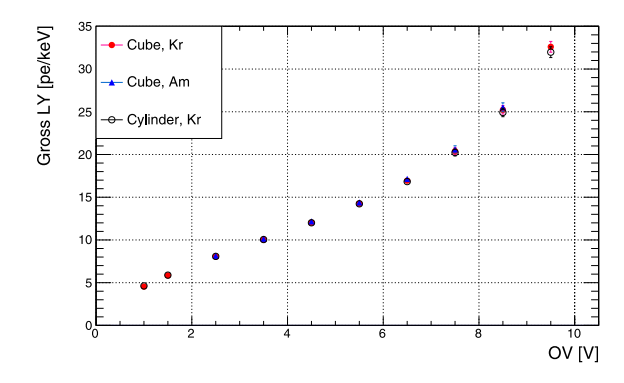


Fig. 3. (Left) 83mKr photo-electron spectrum (blue) and background (red) at 5.5 OV; (Right) Gross light yield of both chambers as a function of the applied OV.



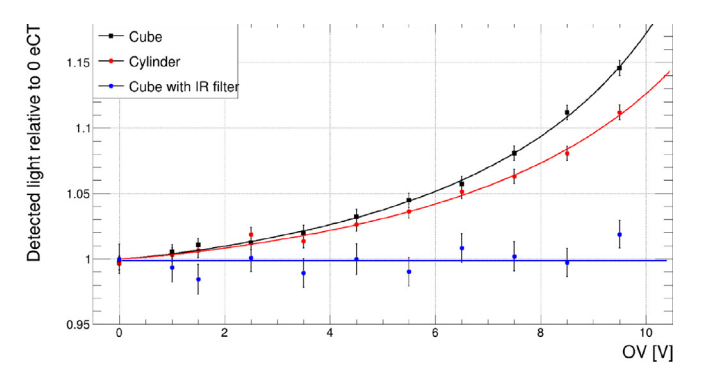


Fig. 4. (Left) Cubic chamber with the colored glass windows installed in place of the fused-silica windows; (Right) eCT contribution vs. SiPM OV. The plot shows the gross LY observed by the top photo-detector (fixed at 8.5 OV) in both chambers, for different operating OVs of the bottom photo-detector. The LY is scaled with respect to 0 OV of the source photo-detector.

We assume  $\lambda_{i\text{CT}}$ , physically interpreted as the mean number of iCT generated directly from a single avalanche, to be proportional to the charge gain of the SiPM, G, and to the PDE for iCT photons,  $\epsilon_R$ , i.e.  $\lambda_{i\text{CT}} = a_{i\text{CT}} \cdot G \cdot \epsilon_R$ . The proportionality constant  $a_{i\text{CT}}$  represents the acceptance for iCT photons i.e. it is the probability for a CT photon to be absorbed in the silicon bulk before escaping. We adopt the model of the gain,  $G = k \cdot (V - V_{\text{bd}}^{\text{C}})$ , and of the PDE,  $\epsilon_R = \eta \cdot [1 - e^{-(V - V_{\text{bd}}^{\text{A}})/V_h}]$  as a function of the OVs [5], with the constants k and  $\eta$ . Considering that red/infrared photons are dominant in oCT, only hole-driven avalanches are taken into account, which is a reasonable approximation for the NUV SiPMs. These lead to the following expression:

$$\lambda_{\rm iCT} = \xi_{\rm iCT} \cdot (V - V_{\rm bd}^{\rm C}) \cdot [1 - e^{-(V - V_{\rm bd}^{\rm A})/V_{\rm h}}],$$
 (1)

where  $\xi_{\text{iCT}} = k \cdot \eta \cdot a_{\text{iCT}}$  is referred to as the acceptance parameter.

Furthermore, we parametrize the observed variance as  $Var[n] = F_{iCT} \cdot \langle n \rangle$  with the generalized Fano factor,  $F_{iCT}$ , effectively parametrized as  $F_{iCT} = \delta \cdot (1 - \lambda_{iCT})^{\alpha}$  [5].

#### 4.3. External cross-talk

The eCT contribution was measured by observing the relative increase in the amount of light seen by the top (target) photo-detector (operated at 8.5 OV) for different OVs of the bottom (source) photo-detector, as shown by the black and the red data points in Fig. 4. Since the emission of CT photons occurs in the red/infrared region, as reported in Ref. [7], their propagation across the detector volume can, in principle, be inhibited by introducing infrared filters. For this purpose, two FGB37S colored glass windows [8] of dimensions (50  $\times$  50  $\times$  2 mm³) were acquired from THORLABS. They were coated with TPB and installed in the cubic chamber in place of the fused-silica windows. These windows have a peak transmission efficiency of 90% at 500 nm, and have almost zero transmission above 700 nm. The blue points in the right plot of Fig. 4 show the measurement results with these windows, demonstrating the suppression of the eCT contribution.

# 5. Analytical model

When the detector system involves only a single SiPM array, we consider only iCT and fCT. Analogous to the parametrization discussed in Section 4.2, an incidence of  $n_{\rm ph}$  scintillation photons on the SiPM array results in the mean number of N observed photo-electrons which can be expressed as  $N=n_{\rm ph}\cdot \epsilon_{\rm B}\cdot \mu$ , where  $\epsilon_{\rm B}$  is the PDE for the photon wavelength. The mean CT amplification  $\mu$  can be given as  $\mu=1/(1-\lambda_{\rm iCT}-\lambda_{\rm fCT})$ , where  $\lambda_{\rm iCT}+\lambda_{\rm fCT}\ll 1$ . As the emission and detection of the iCT and fCT occur on the same SiPM array,  $\lambda_{\rm iCT}$  and  $\lambda_{\rm fCT}$  can be expressed with two acceptance parameters as

$$\lambda_{\text{iCT}} + \lambda_{\text{fCT}} = (\xi_{\text{iCT}} + \xi_{\text{fCT}}) \cdot (V - V_{\text{bd}}^{\text{C}}) \cdot [1 - e^{-(V - V_{\text{bd}}^{\text{A}})/V_{\text{h}}}].$$
 (2)

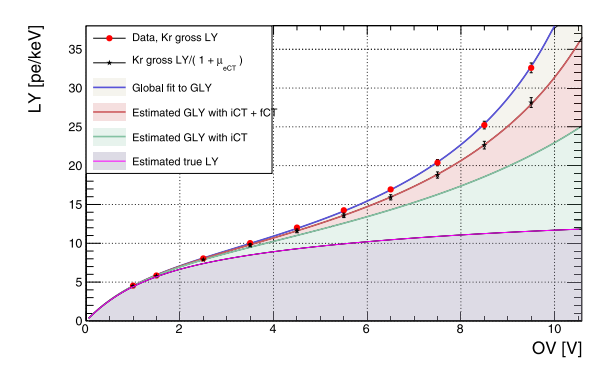
When the system involves two similar SiPM arrays (1 and 2), the mean number of photo-electrons observed by each can be expressed as

$$\begin{split} N_1 &= (n_{\text{ph}1} \cdot \varepsilon_{\text{B1}} + \lambda_{21} \cdot N_2) \cdot \mu_1 \\ N_2 &= (n_{\text{ph}2} \cdot \varepsilon_{\text{B2}} + \lambda_{12} \cdot N_1) \cdot \mu_2 \end{split} \tag{3}$$

where  $\mu_1$  and  $\mu_2$  are the mean amplifications by iCT+fCT in the SiPM array 1 and 2, respectively. Similarly, the number in the subscript represents parameters for the corresponding SiPM array. The eCT can be generated by the SiPM array 1 and detected by 2, or vice versa, and  $\lambda_{12}$  and  $\lambda_{21}$  describe these two cases, respectively. When the two SiPM arrays operate at different voltages ( $V_1$  and  $V_2$ ),  $\lambda_{12}$  can be expressed as  $\lambda_{12} = \xi_{12} \cdot (V_1 - V_{\rm bd}^{\rm C}) \cdot [1 - e^{-(V_2 - V_{\rm bd}^{\rm A})/V_{\rm h}}]$ . For a symmetric arrangement of the two SiPM arrays, we assume  $\xi_{12} = \xi_{21} = \xi_{\rm eCT}$ . Assuming also  $n_{\rm ph1} = n_{\rm ph2} = n_{\rm ph}$ , Eq. (3) lead to

$$N_1 = \frac{n_{\rm ph} \cdot \mu_1(\varepsilon_{\rm B1} + \lambda_{21} \cdot \varepsilon_{\rm B2} \cdot \mu_2)}{1 - \lambda_{21} \cdot \lambda_{12} \cdot \mu_1 \cdot \mu_2}.\tag{4}$$

In this way  $\xi_{\text{eCT}}$  is separately accessible, as demonstrated in Section 4.3. Note that, when the two detectors operate at the same voltage, Eq. (4)



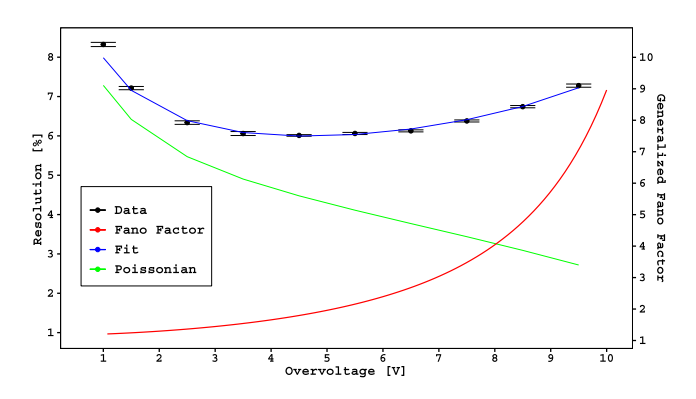


Fig. 5. (Left) Breakdown of the oCT components in the measured  $LY_G$  for the cubic chamber with  $^{83m}$ Kr. The magenta line represents the estimated true light yield as a function of the OV; (Right) Energy resolution of the cubic chamber (data points in black) as a function of the OV. The solid blue line represents the fit to the data points using the resolution fit [5]. The solid green line shows the expected Poisson resolution and the red curve shows the calculated generalized Fano factor (relative to the axis scale on right).

reduces to  $N = n_{\rm ph} \cdot \varepsilon_{\rm B}/[1-(\lambda_{\rm iCT}+\lambda_{\rm fCT}+\lambda_{\rm eCT})]$ , being sensitive only to the sum of the three acceptance parameters:  $\xi_{\rm oCT}=\xi_{\rm iCT}+\xi_{\rm fCT}+\xi_{\rm eCT}$ .

Fig. 5 (Left) shows the fit of the analytical model to LY<sub>G</sub> (Ref. [5], Table 1 therein) for the cubic chamber with  $^{83\text{m}}$ Kr. From the fit,  $\xi_{\text{oCT}}$  and the net light yield, LY =  $n_{\text{ph}} \cdot \varepsilon_{\text{B}} / E$  (E=41.5 keV), can be derived. We adopt the model,  $\varepsilon_{\text{B}} = \eta \cdot [\zeta \cdot (1-e^{-(V-V_{\text{bd}}^A)/V_{\text{e}}}) + (1-\zeta) \cdot (1-e^{-(V-V_{\text{bd}}^A)/V_{\text{h}}})]$  with the relative fraction of the electron-driven avalanches,  $\zeta$  [5]. LY =  $12 \pm 1$  pe/keV is estimated at 9.5 OV. With  $\xi_{\text{iCT}}$  and  $\xi_{\text{eCT}}$  determined in the measurements in Sections 4.2 and 4.3 respectively, the rest of  $\xi_{\text{oCT}}$  is attributed to  $\xi_{\text{fCT}}$ , yielding the ratio:  $\xi_{\text{iCT}} : \xi_{\text{fCT}} : \xi_{\text{eCT}} \sim 1 : 0.28 : 0.15$ . The different color bands thus represent the obtained breakdown of different oCT components. The model is validated by the fact that the parametrizations of  $\lambda_{\text{oCT}}$  obtained from the LY<sub>G</sub> fit and of the effective model of the generalized Fano factor well describe the OV dependence of the measured energy resolution, right plot of Fig. 5.

#### 6. Conclusions

In this work we presented the measurements of light yield, energy resolution, and eCT in two prototype LAr chambers with SiPM-based readout. An analytical model involving the OV dependence of the PDE and of the oCT was developed to explain the observed detector response. In conjunction with the results obtained from the dedicated measurements of iCT, the model was parametrized to well describe the gross light yield and the energy resolution simultaneously. After deconvolving the contributions of oCT components the net light yield of the system was estimated to be  $12\pm1$  pe/keV at 9.5 OV, which is one of the best light yield values in a LAr setup. However, at the same time, the energy resolution was found to be significantly compromised due to the dominance of oCT at high OVs. Therefore, the operating OV of the SiPMs is to be determined considering the LY and the energy resolution, and a careful simulation study is required for that. It will most likely be in the (6–7) OV range.

To mitigate the impact of eCT, optical filters that block the wavelength of CT photons, were introduced in the detector volume. The eCT measurements demonstrated that these filters are able to suppress the

eCT photons. This is an important information that can be of use in the designing of future detectors with SiPM-based readouts.

# Declaration of competing interest

The authors declare that they have no known competing financial interests or personal relationships that could have appeared to influence the work reported in this paper.

# Acknowledgments

We acknowledge support from the Istituto Nazionale di Fisica Nucleare (Italy) and Laboratori Nazionali del Gran Sasso (Italy) of INFN, from NSF (US, Grant PHY-1622415 and PHY-1812540 for Princeton University, USA), from the Royal Society UK and the Science and Technology Facilities Council (STFC), UK, part of the United Kingdom Research and Innovation, from the European Union's Horizon 2020 research and innovation programme under grant agreement No 952480 (DarkWave project), and from the International Research Agenda Programme AstroCeNT (MAB/2018/7) funded by the Foundation for Polish Science (FNP), Poland from the European Regional Development Fund.

#### References

- A.L. Lacaita, F. Zappa, S. Bigliardi, M. Manfredi, IEEE Trans. Electron Devices 40 (3) (1993) 577–582, 1993.
- [2] A.N. Otte, Nucl. Instrum. Methods Phys. Res. A 610 (2009) 105–109.
- [3] S. Vinogradov, Nucl. Instrum. Methods Phys. Res. A 695 (2012) 247, http://dx.doi.org/10.1016/j.nima.2011.11.086.
- [4] S. Vinogradov, T. Vinogradova, V. Shubin others, IEEE Nuclear Science Symposium Conference Record, NSS/MIC, 2009, pp. 1496–1500, http://dx.doi.org/10.1109/ NSSMIC.2009.5402300.
- [5] M.G. Boulay, et al., arXiv:2201.01632 [physics.ins-det].
- [6] M.G. Boulay, et al., Eur. Phys. J. C 81 (12) (2021) 1099, http://dx.doi.org/10. 1140/epjc/s10052-021-09870-7, arXiv:2106.15506 [physics.ins-det].
- [7] R. Mirzoyan, et al., Nucl. Instrum. Methods Phys. Res. A 610 (2009) 98–100, http://dx.doi.org/10.1016/j.nima.2009.05.081.
- [8] https://www.thorlabs.com/thorproduct.cfm?partnumber=FGB37S.